Magnetism and Faraday Rotation in Oxygen-Deficient Polycrystalline and Single-Crystal Iron-Substituted Strontium Titanate

Taichi Goto, Dong Hun Kim, Xueyin Sun, Mehmet C. Onbasli, Juan M. Florez, Shyue Ping Ong, Patricio Vargas, Karl Ackland, Plamen Stamenov, Nicolas M. Aimon, Mitsuteru Inoue, Harry L. Tuller, Gerald F. Dionne, J. Michael D. Coey, and Caroline A. Ross

Phys. Rev. Applied **7**, 024006 — Published 8 February 2017

DOI: 10.1103/PhysRevApplied.7.024006

Magnetism and Faraday Rotation in Oxygen-Deficient Polycrystalline and Single-Crystal Iron-Substituted Strontium Titanate

Taichi Goto,[1,*] Dong Hun Kim,[2] Xueyin Sun,[3] Mehmet C. Onbasli,[4] Juan M. Florez,[5] Shyue Ping Ong,[6] Patricio Vargas,[5] Karl Ackland,[7] Plamen Stamenov,[7] Nicolas M Aimon,[4] Mitsuteru Inoue,[1] Harry L. Tuller,[4] Gerald F. Dionne,[4] J. Michael D. Coey,[7] and Caroline A. Ross[4,**]

[1]Department of Electrical and Electronic Information Engineering, Toyohashi University of Technology, 1-1 Hibari-Ga-Oka, Tempaku, Toyohashi 441-8580 (Japan)
[2]Department of Materials Science and Engineering, Myongji University, 116 Myongji-ro, Cheoin-gu, Yongin, Kyeonggi-do 449-728 (Korea)
[3]School of Materials Science and Engineering, Harbin Institute of Technology, 92 West Dazhi Street, Nan Gang District, Harbin 150001 (China)
[4]Department of Materials Science and Engineering, Massachusetts Institute of Technology, 77 Massachusetts Avenue, Cambridge, Massachusetts 02139 (USA)
[5]Departamento de Física, Universidad Técnica Federico Santa María, España 1680, Valparaíso, P.O. Box 110-V (Chile)
[6]Department of NanoEngineering, University of California, San Diego, 9500 Gilman Dr, La Jolla, California 92093 (USA)
[7]School of Physics, Trinity College Dublin, College Green, Dublin 2 (Ireland)
*goto@ee.tut.ac.jp, **caross@mit.edu

KEYWORDS: perovskite, Faraday rotation, nanorod, magneto-optical, oxygen vacancy

ABSTRACT

Both polycrystalline and single-crystal films of iron-substituted strontium titanate, $Sr(Ti_{0.65}Fe_{0.35})O_{3-\delta}$, prepared by pulsed laser deposition (PLD), show room temperature magnetism and Faraday rotation (FR), with the polycrystalline films exhibiting higher saturation magnetization and FR. The magnetic properties vary with the oxygen pressure at which the films are grown, showing a maximum at pressures of ~4 μTorr at which the unit cell volume is largest. The results are discussed in terms of the oxygen stoichiometry and corresponding Fe valence states, the structure and strain state, and the presence of small volume fractions of metallic Fe in single-crystal films grown at the optimum deposition pressure. Integration of magneto-optical polycrystalline films on an optical waveguide device demonstrates a nonreciprocal phase shift.

I. INTRODUCTION

Complex oxides exhibit a wide range of useful properties such as high temperature superconductivity, ferroelectricity, colossal magnetoresistance, magnetism, magneto-electricity, magneto-optical activity, and multiferroicity that have inspired spintronic, magnetoelectronic, and optical applications [1-6]. Transition-metal-substituted perovskites or perovskite-derived structures are particularly interesting because their properties can be tuned by cation substitution over extensive composition ranges, and because they can be epitaxially grown on a buffered Si substrate [7-10]. Beyond cation composition, the properties are also very sensitive to the growth conditions and substrate used, which affect the microstructure, film strain [7], oxygen deficiency, the cation valence states, and the ordering of cations within the A and B sites.

Iron-substituted strontium titanate or $SrTi_{1-x}Fe_xO_{3-\delta}$ (STF) (here δ represents the oxygen deficiency with respect to a stoichiometric perovskite $SrTi_{1-x}Fe_xO_3$, i.e., one in which the Fe is present as Fe^{4+}) has been extensively characterized as a mixed electronic-ionic conductor [11-15] and for its magnetic, magneto-optical, ferroelectric, and catalytic properties [16-19]. Characterization of STF has included determining its oxygen content via thermogravimetric analysis and coulometric titration [20,21], and measurements of ionic/electronic conductivity and impedance [12,13,15,22-24]. The magnetic properties are believed to be related to oxygen vacancies [16,20,25], although the origin of the magnetism is not fully understood. We have previously found that epitaxial STF and $Sr(Ti_{1-x}Co_x)O_{3-\delta}$ (STCo) films on $SrTiO_3$ (STO), $LaAlO_3$, and CeO_2/yttria-stabilized zirconia (YSZ)-buffered (001) Si substrates grown in vacuum with $x = 0.1$ to 0.5, i.e. non-dilute systems, exhibited room-temperature magnetism and anisotropy with an out-of-plane magnetic easy axis that was attributed to magnetoelastic effects [16,17,26-28]. However, films deposited in oxygen had no significant room-temperature magnetism. The magnetic moment of vacuum-deposited epitaxial STF films persisted to a tempera-

ture of >1000°C and the magnetization decreased slowly as a function of temperature [16,29,30]. Depending on the thickness and deposition conditions, STF could be grown as a single crystal film on STO, or as a double epitaxial film consisting of an (001)-oriented STF film with (011)-oriented crystals growing within it, both orientations being epitaxial with the substrate [31]. The single crystal and double epitaxial microstructures differed in their strain state, uniformity of the Fe distribution, and magnetic properties [19,31].

These experimental results led to the conclusion that strain and oxygen stoichiometry were key structural factors in determining the magnetic properties of the STF and STCo films (factors that are also important in many other oxide systems [29,32],) but there are few reports on the effect of oxygen pressure during growth [33,34], and polycrystalline films have not been investigated. We report on the correlations among the microstructure, valence, and distribution of the Fe ions as well as the room temperature magnetic properties of STF films as a function of base pressure P, characterized by high-resolution x-ray diffraction (XRD), transmission electron microscopy (TEM), Faraday rotation (FR), magnetometry, and Mössbauer spectroscopy. The STF films on Si were polycrystalline but exhibited a magnetic moment and FR up to 65% higher than the single-crystal film deposited on an STO substrate. From the viewpoint of applications, the formation of polycrystalline magnetic perovskite films on silica or other non-epitaxial substrates allows the useful properties of STF to be easily introduced into complementary metal-oxide semiconductor (CMOS) devices and into optical devices such as isolators and magnetophotonic crystals [4,35-39], spatial light modulators [40-42], or magneto-optical holographic memories [43-46]. First-principles calculations demonstrate the importance of oxygen defects and exchange interactions in determining the magnetic properties.

II. FILM GROWTH AND CHARACTERIZATION

A. Film preparation

In this work, STF films were fabricated on silicon covered by a native oxide and on STO substrates under various P using pulsed laser deposition (PLD). The $SrTi_{0.62}Fe_{0.38}O_{3-\delta}$ target was prepared using a conventional mixed oxide sintering method [47]. During film deposition, the KrF excimer laser (wavelength $\lambda = 248$ nm) was pulsed at a frequency of 10 Hz with a pulse duration of 25 ns. The spot size on the target was 0.5 mm × 2.0 mm, and the energy density at the target surface was ~1.3 J cm^{-2} during the pulse. The deposition rate was 1.8–2.7 nm min^{-1}. STF films of thickness 70 ± 10 nm were deposited by PLD onto 0.38-mm-thick double-side-polished (001) Si substrates and onto 0.5-mm-thick double-side-polished (001) STO substrates. Films were grown simultaneously on both substrate types in each deposition run. The substrates were placed 80 mm from the target, and the substrate holder was heated to 650°C and was rotated for uniform growth. This temperature was chosen to minimize the formation of secondary phases such as iron oxides. Samples were prepared at a range of base pressures below 10 μTorr by pumping the chamber until a specific base pressure P was reached. The substrate was then heated, which raised the total pressure of the chamber to about 30 μTorr due to chamber outgassing. The chamber pressure was then pumped back down to P before deposition started. Therefore the pressure P during deposition consists of residual gas which includes oxygen and water vapor. Pre-deposition (5×10^3 laser pulses) was started with the shutter placed between the PLD target and the substrate, leading to an increase in the total chamber pressure by ~2 μTorr. After opening the shutter for film deposition (2×10^4 pulses), the chamber pressure gradually decreased and returned to near P at the end of the deposition. The substrate was cooled to room temperature at a rate of –5°C min^{-1} while pumping the chamber.

B. X-ray characterization

In-plane and out-of-plane lattice constants of single crystalline films on STO and polycrystalline films on Si were characterized by XRD (PANalytical, X'Pert) and two high-resolution XRD systems (HRXRD, Bruker-Axs D8 DISCOVER and Rigaku Smartlab). XRD patterns are shown in Figs. 1(a) and 1(b) for STF/STO and STF/Si, taken using a Cu-Kα radiation source at a wavelength of 0.15418 nm. Figure 1(a) was measured by XRD (PANalytical, X'Pert), in which $K\beta_1$ peaks from the Cu source were observed. Figure 1(b) was measured by HRXRD (Rigaku Smartlab). The STF/Si samples were tilted by 1° to eliminate the strong substrate peak. The out-of-plane lattice parameters of STF on STO and on Si, $c_{STF/STO}$ and $c_{STF/Si}$, varied with the deposition pressure, and exhibited a maximum at P = 3 - 4 μTorr, with the variation stronger for the STF/STO. This behavior was also confirmed with the (002) peak obtained from XRD (PANalytical X'Pert). The TiO_2 (202) peak in Fig. 1(a) originated from the substrate.

Reciprocal space mapping (RSM) was used to measure the in-plane lattice parameter $a_{STF/STO}$ for the STF/STO. Grazing incidence diffraction (GID) was used to measure $a_{STF/Si}$ for the STF/Si samples grown at P = 1, 4, and 10 μTorr with the incident angle of the x-rays ω fixed at 0.4°. Figure 1(c) shows the RSM data for the STF/STO samples for the asymmetric (310) peak. The intense upper peak arises from diffraction from the STO substrate, and the bottom peak corresponds to the STF films. Multiple peaks are attributed to twinning of the substrates. The film and substrate peaks align in q_x indicating coherent cube-on-cube epitaxial growth of the STF films on the STO substrate, i.e. $a_{STF/STO} = a_{STO}$, whereas q_z gives the out-of-plane lattice parameter c, which differs for the film and substrate. The RSM data gave a standard deviation of < 10^{-3} Å for $a_{STF/STO}$. The difference in values for c from different diffractometers, given by (HRXRD value – XRD value) / HRXRD value, was less than 0.1%, and the value of $c_{STF/STO}$ from RSM matched that measured by XRD. All the STF films on STO had out-of-plane lattice parameters greater than that of STO (a_{STO} = 3.905 Å) and were tetragonally distorted, with $(c/a)_{STF/STO}$ = 1.013 to 1.030 indicating an in-plane compressive strain in the STF, similar to that found in prior work [16]. Figure 1(d) shows the variation of $a_{STF/STO}$, $c_{STF/STO}$, and unit cell volume $V_{STF/STO}$ with base pressure P.

For the samples of STF/Si, the in-plane and out-of-plane lattice parameters, $a_{STF/Si}$ and $c_{STF/Si}$, and the unit cell volume $V_{STF/Si}$ are shown in Fig. 1(d). The data gave a standard deviation of ~6×10^{-4} Å for a, and 2×10^{-3} Å for c. The value of $a_{STF/Si}$ was 3.955 ± 0.003 Å and showed little variation with P. Of the three STF/Si samples whose unit cell volume was measured, the one

grown at P = 4.0 μTorr showed the largest unit cell volume, the same trend as for films on the STO substrate. The value of $c_{STF/Si}$ was similar to or slightly smaller than $a_{STF/Si}$, i.e. $(c/a)_{STF/Si}$ = 0.990 to 0.998, depending on P. Thermal mismatch on cooling would lead to a tensile strain in the STF/Si film (c/a < 1), since Si has a lower thermal expansion coefficient than STF. This differs from the films on STO where lattice mismatch governs the strain state and produces an in-plane compressive strain in the STF, with c/a > 1.

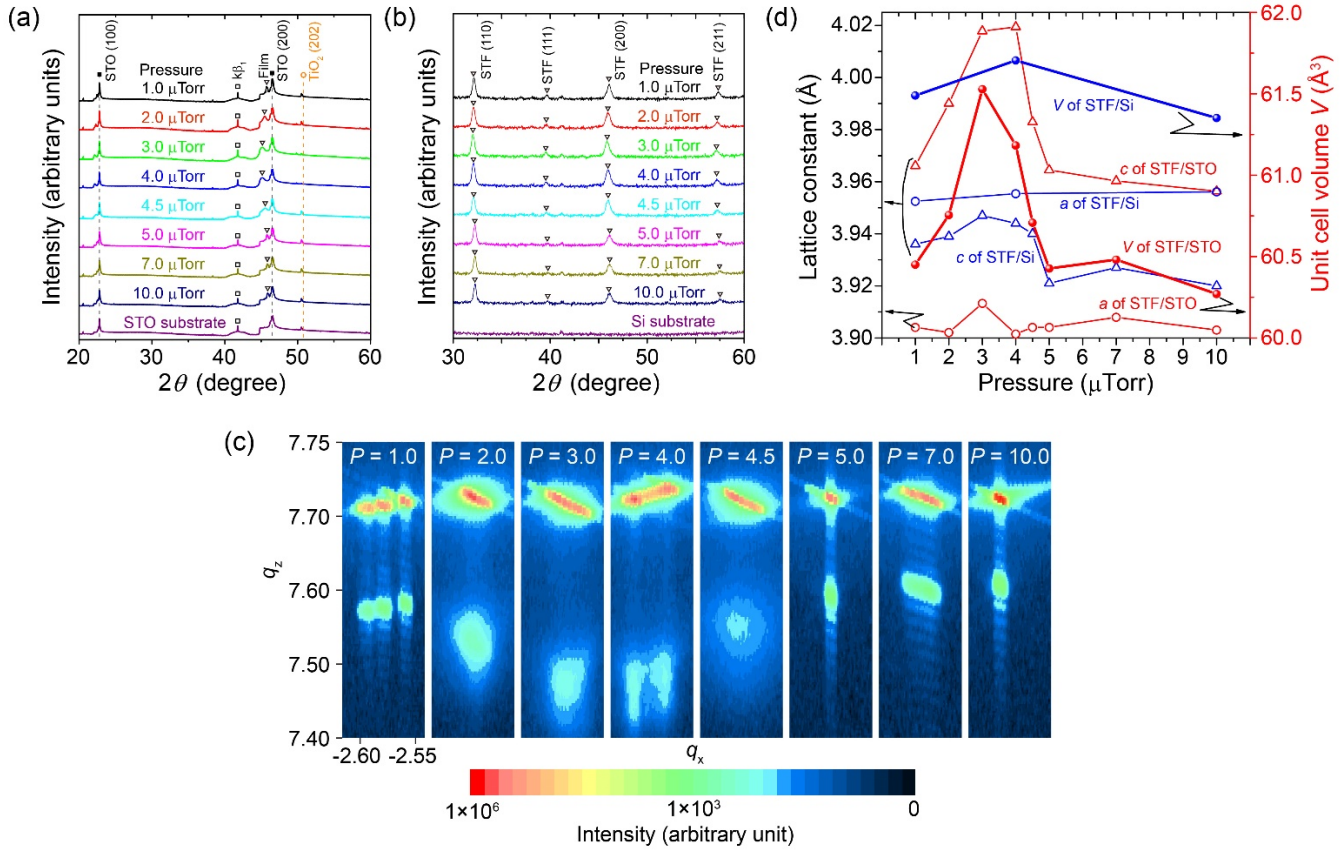

FIG. 1. Structural analysis of the STF films with XRD. (a) XRD patterns of STF/STO. The triangles show the film peaks. Black squares are peaks from bulk STO. A circle shows a TiO_2 peak present in the substrate scan. (b) XRD patterns of STF/Si. Positions of STF peaks are shown with triangles. There are no Si peaks in this angular range. (c) Reciprocal space mapping of single crystalline STF on STO substrate, plotted in q_z–q_x for the asymmetric (310) peak. (d) Lattice constants and unit cell volumes of STF films versus deposition pressure for both STF/STO and STF/Si.

The larger unit cell volume of the films compared to that estimated for bulk STF without oxygen vacancies [$SrTi_{0.65}Fe_{0.35}O_3$, V = ~60.13 Å^3 interpolated linearly from the unit cell volumes of STO (a = 3.9051 Å, V = ~59.55 Å^3) [48] and $SrFeO_3$ (a = 3.9410 Å, V = ~ 61.21 Å^3) [49] is a result of the greater oxygen vacancy content in the films compared to the bulk, which drives the Fe to lower valence states, expanding the lattice because of the larger ionic radii of the Fe. Other work on STO films [50] has showed changes in cation stoichiometry and hence lattice parameter at different laser focus conditions, but here we kept the deposition conditions nominally the same except for the base pressure, so we attribute changes in lattice volume to the oxygen vacancies and corresponding changes in Fe ionic radius. MacChesney *et al.* and Taguchi *et al.* showed that oxygen vacancies in $SrFeO_{3-\delta}$ and $SrCoO_{3-\delta}$ respectively increased the unit cell volume [51,52], and a sufficiently large oxygen deficiency (δ > 0.12) promoted a cubic-to-tetragonal structural change in $SrFeO_{3-\delta}$ [42]. Perry *et al*. showed that the largest lattice parameter is obtained for STF annealed under the most reducing conditions, based on chemical expansion measurements [34]. Chakraverty *et al.* demonstrated that, for $SrFeO_{2.5}$ films on STO grown by PLD, the laser spot size, which affects the growth process, kinetics and stoichiometry, controlled the lattice parameter [53].

C. Film morphology.

Cross-sectional TEM images of STF/Si and STF/STO grown at P = 1, 4 and 10 μTorr are given in Fig. 2. All three STF/Si films had a polycrystalline columnar microstructure, and energy-dispersive x-ray spectroscopy (EDX) mapping of the 4 μTorr sample, Fig. 3, indicates a spatial variation in the Fe content, with higher Fe content corresponding to a few of the columnar features. In

agreement with the Mössbauer spectroscopy (described below), there was no clear evidence from high resolution TEM that these columns were metallic Fe, and we presume they represent STF with a higher Fe content than neighboring grains. A similar inhomogeneity was found at P = 1 μTorr, but at 10 μTorr the Fe was uniformly distributed. The compound $SrTi_{1-x}Fe_xO_{3-\delta}$ is stable throughout the composition range [13,14], therefore we assume that the inhomogeneity is different in origin from that seen in spinodal decomposition such as that of Cr-rich (Zn, Cr)Te [54], In-rich (Ga, In)N [55], or (Mn, Ga)As [56] systems. In comparison, the STF grown on STO was single-crystal but showed contrast that indicated small scale structural inhomogeneity, possibly representing layered vacancy ordering as seen in brownmillerite-structured $SrFeO_{2.5}$ [57] and in $(La,Sr)CoO_3$ [58,59]. At P = 4 μTorr, a few straight, vertical nanopillars were observed perpendicular to the substrate within the perovskite matrix. Lattice imaging revealed that the pillars were metallic α-Fe. The pillars were sparsely distributed, with spacings of ~200 nm in the TEM image of a lamella ~20–50 nm thick. This suggests a density of 100–250 pillars per μm^2.

The pillar width was 3–5 nm, giving an estimate of the volume fraction of metallic Fe of 0.1–0.4%. This volume fraction is small, but it could contribute a significant amount of the net magnetization because metallic Fe has a high saturation magnetization of 1700 emu cm^{-3}. However, the majority of the Fe remains in the perovskite, e.g. the formation of even 0.5 vol.% metallic Fe would deplete Fe from ~8% of the STF volume. Films grown on STO at P = 1 μTorr and 10 μTorr had no pillars, and the Fe was uniformly distributed.

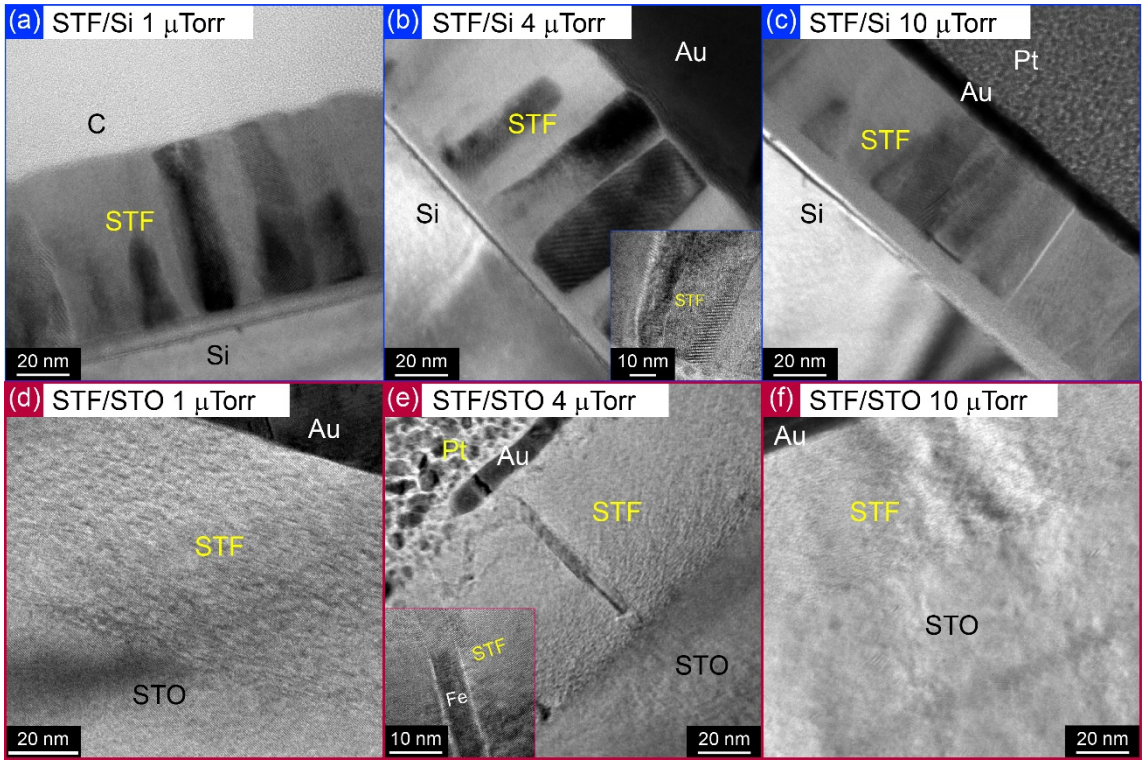

FIG. 2. Transmission electron microscopy of STF samples. Cross-sectional TEM images of STF/Si deposited at P = (a) 1 μTorr, (b) 4 μTorr, and (c) 10 μTorr. Cross-sectional TEM images of STF/STO deposited at P = (d) 1 μTorr, (e) 4 μTorr, showing a Fe rod, and (f) 10 μTorr. Specimens were covered with conductive materials, either Au or C.

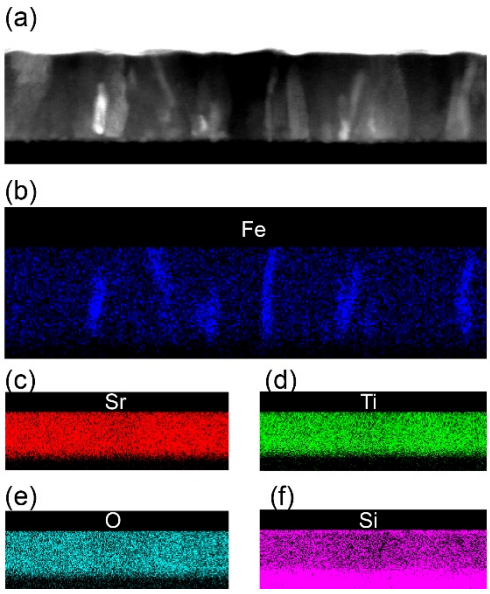

FIG. 3. Composition analysis of STF/Si. (a) STEM images and STEM-EDX element mappings of STF deposited on Si at P = 4 μTorr. STEM-EDX Element map of (b) Fe, (c) Sr, (d) Ti, (e) O, (f) Si. A Sr peak overlaps the Si peak leading to a false signal for the region of the film in (f).

D. Fe valence state.

Measurement of the atomic ratio of Ti and Fe is shown in Fig. 4(a) from energy-dispersive x-ray spectroscopy (EDS, FEI Philips XL 30), confirming that there was no systematic change in the ratio of Fe:Ti (= 0.35:0.65) with P.

The Fe valence state was characterized by conversion electron Mössbauer spectrometry (CEMS) and by x-ray photoelectron spectroscopy (XPS). CEMS showed a difference between two films grown at P = 2 μTorr on different substrates, as shown in Figs. 4(c), and 4(d). For the STF/Si, a weak paramagnetic signal of Fe^{3+} was detected (~0.7% max emission). The signal may be fitted to a singlet (Gaussian) or a doublet (2 pseudo-Voigts) as shown in Fig. 4(c), yielding an isomer shift relative to α-Fe of 0.25 ± 0.04 mm s^{-1} and a quadrupole splitting of 0.89 ± 0.08 mm s^{-1}. This signal may arise from Fe^{3+} associated with oxygen vacancies [60]. No other signals were resolved.

The STF/STO showed 0.5–0.6 % emission after optimization. Unlike the sample on Si, the STF/STO showed a metallic iron magnetic phase, identified not just because of the presence of a sextet but also because of the isomer shift of 0.00 ± 0.02 mm s^{-1}, equal to that of α-Fe (Fig. 4(d)). The peak-intensity ratio of the sextet state indicates that the iron is not uniformly magnetized perpendicular to the substrate [61-63]. There was also a paramagnetic ferric doublet with an isomer shift of 0.35 ± 0.04 mm s^{-1} that accounted for 23% of the peak area. A measurement using Auger electrons sensitive to the top 20–30 nm of the film showed a lower peak area fraction (15%) for the paramagnetic iron suggesting a depth dependence of the iron valence state. These results indicate that metallic Fe was present in the STF/STO but not in the STF/Si grown at P = 2 μTorr.

Figure 4(b) shows XPS results in which the Fe peaks were similar over the range of deposition pressures and the two substrate types. The peak positions were calibrated so that the Cu peak was present at 284.8 eV. There were no significant differences in the Sr, Ti, and O XPS peaks. The satellite peaks around the Fe $2p_{3/2}$ and $2p_{1/2}$ doublet indicate the presence of Fe^{3+} but not Fe^{2+}, similar to epitaxial $BiFeO_3$ [64] and iron oxides [65]. The lack of a metallic Fe peak in the 4 μTorr sample on STO differs from the TEM results and from the Mössbauer analysis of the P = 2 μTorr sample. Since XPS is surface-sensitive, we assume that the top parts of the Fe nanorods at the surface would be subject to oxidation, or their very small area coverage may have precluded the observation of a metallic Fe peak.

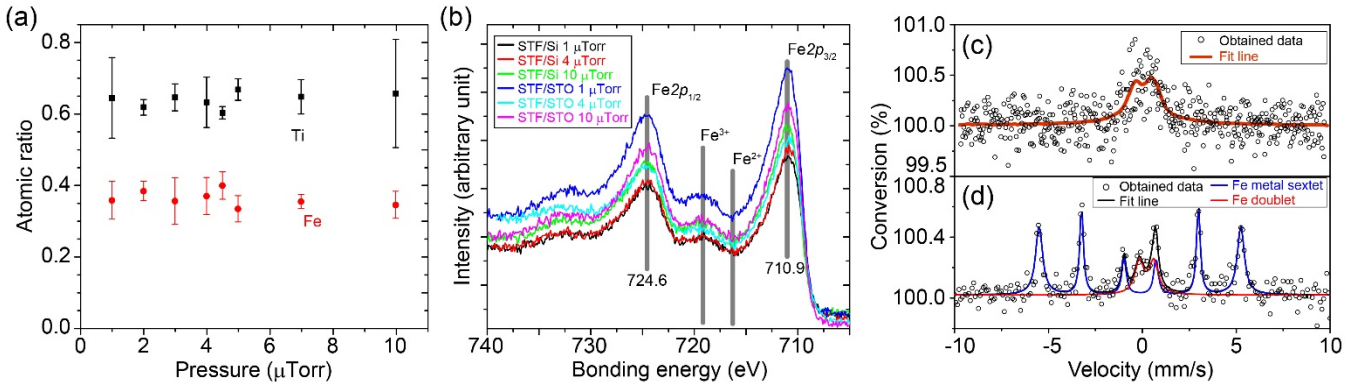

FIG. 4. Composition analysis of the STF films. (a) Atomic ratio of Fe to Ti in STF/STO measured by EDS. Error bars show the standard deviation. (b) XPS peaks from Fe 2*p* in STF films on STO and Si substrates. Mössbauer spectroscopy of (c) STF/Si, and (d) STF/STO, both deposited at $P = 2$ μTorr, measured over the depth of the films. The STF film on the Si substrate does not show the metal sextet phase, but instead, a weak paramagnetic signal.

E. Optical and magnetic characterization

Transmissivity of the films on the two substrates from visible to near-IR wavelengths is shown in Fig. 5. For energies below the bandgap, the transmissivity of STF/Si was higher than that of bare silicon because of the anti-reflection effect that arises from introducing a lower refractive index film on a higher refractive index substrate. The transmissivity of STF/STO and bare STO were similar except for energies just below the bandgap where the STF/STO became absorbent.

Atomic force microscope (AFM) images of the STF/Si and STF/STO grown at $P = 4$ μTorr are shown as insets in Fig. 5. The films had a root-mean-square roughness of 1.8 and 2.2 nm, respectively, leading to reflective film surfaces. The STF/Si grown at $P = 1$, 4, and 10 μTorr had similar surface topography, with in-plane feature sizes of 20–40 nm. In contrast, the STF/STO grown at $P = 1$ μTorr and 10 μTorr was much smoother than the film grown at 4 μTorr.

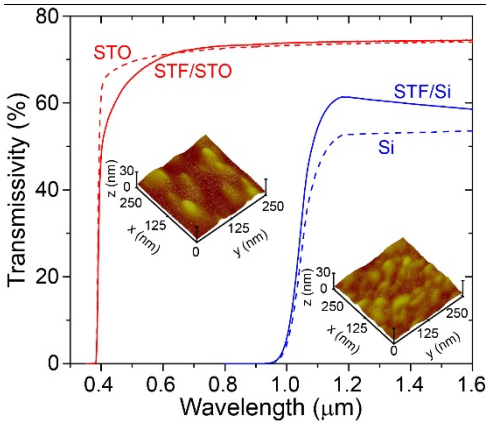

FIG. 5. Optical properties of STF films. Transmission spectra of STF/Si, STF/STO, and their substrates; the insets show the AFM images of the surface topography.

Figure 6 shows the room temperature magnetic hysteresis loops from vibrating sample magnetometry (VSM) for films on both substrates as a function of *P*. Linear substrate signals were subtracted. Uncoated STO substrates subjected to thermal cycling in vacuum in the PLD chamber similar to the thermal cycling during film growth showed a diamagnetic response with little change on annealing. For both substrates, the films grown at $P = 4.0$ μTorr showed the largest saturation magnetization, while films grown at or above $P = 5$ μTorr did not exhibit a hysteresis loop. The magnetic easy axis was along the out-of-plane direction, with switching fields of 3–4 kOe and a high remanence. The hysteresis loop shape, switching field, and the anisotropy field are generally consistent with those seen in previous studies of STF/STO [16,27,28]. The STF/STO grown at $P = 4$ μTorr had $M_s = 17$ emu cm^{-3}, whereas—remarkably—the polycrystalline STF/Si had $M_s = 28$ emu cm^{-3}, which is higher by a factor of nearly two and corresponds to 0.48 μ_B/Fe. In the STF/STO, the metallic Fe would contribute ~2–6 emu cm^{-3} based on the estimated volume fraction.

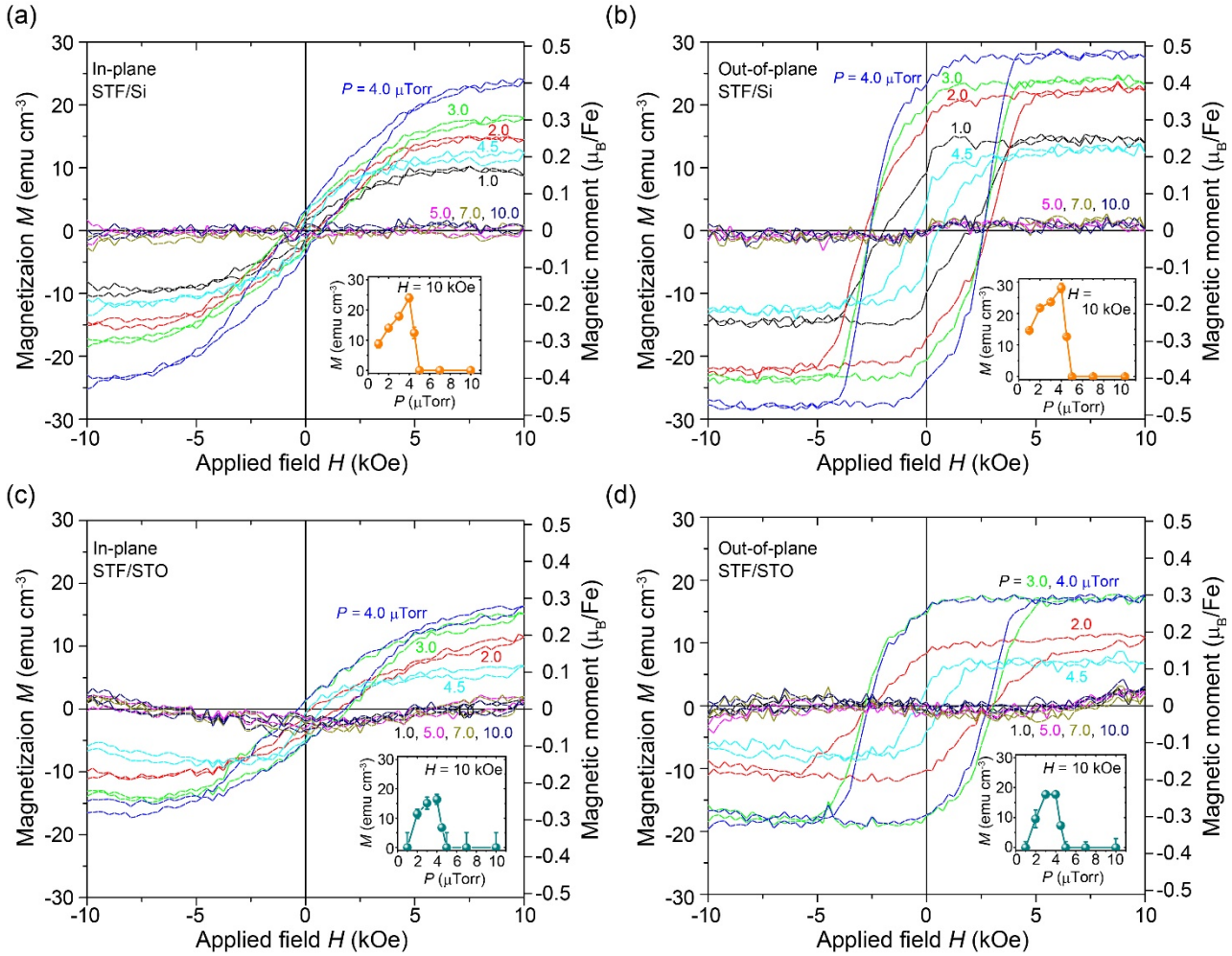

FIG. 6. Magnetic properties of STF films measured by VSM. (a),(b) Magnetic properties of STF/Si specimens (c),(d) Magnetic properties of STF/STO specimens, (a),(c) in-plane and (b),(d) out-of-plane. Insets show the dependence of the magnetization on pressure at $H = 10$ kOe.

The magneto-optical response of STF (FR loop versus applied magnetic field) was measured at a wavelength of 1550 nm by the Faraday cell modulation method [65] and is shown in Fig. 7. The field and light were perpendicular to the film in the Faraday measurement, and the Faraday loop showed a comparable shape and coercivity (~3 kOe) to the out-of-plane magnetic hysteresis loops shown in Fig. 6. Low-spin ($S = 1$, 2 μ_B per ion) Fe^{4+} can provide splitting of the two circular modes of a linearly polarized optical wave required for FR [29]. The saturation FR angle of STF/Si was approximately two times larger than that of STF/STO, reaching –1900 °cm^{-1}, i.e. the FR scaled with the saturation magnetization. This FR is ~60% of that reported for single crystalline cerium-substituted yttrium iron garnet (CeYIG, $Ce_1Y_2Fe_5O_{12}$) [66,67] at 1550 nm. CeYIG is a candidate material for magneto-optical devices in the near-IR. (CeYIG films [4,5,68-70] differ from STF in having an in-plane easy axis.)

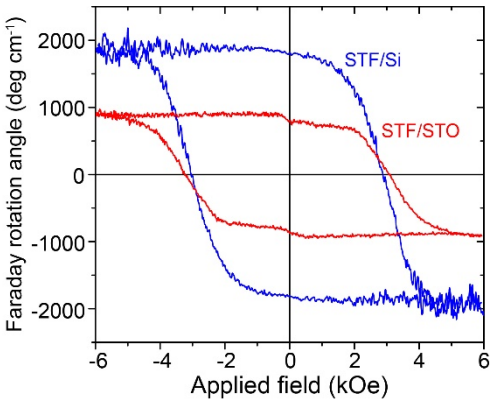

FIG. 7. Magneto-optical properties of STF films. FR loops of STF/Si and STF/STO samples at a wavelength of 1550 nm.

F. Discussion

These results illustrate a sensitivity of the STF structure and the optical and magnetic properties to both the pressure during deposition and the substrate type. Both STO and $SrFeO_3$ structures can accommodate significant amounts of oxygen deficiency, maintaining a perovskite-like structure with oxygen vacancies that may be disordered or that can be arranged in layers, e.g. brownmillerite $SrFeO_{2.5}$ when δ=0.5. The unit cell volume increases with δ and there are dramatic changes in conductivity and other properties with δ [11,15,20,22-24,72]. Vacancies can even be introduced into an STO substrate at low pressure and high temperature [73], which affects the surface of the substrate prior to film growth.

The oxygen content of the films and therefore δ is difficult to quantify because the sample volume is too small for thermogravimetric analysis, although other methods such as photoluminescence, direct imaging, or measurements of cation valence may be applicable [74,75]. However, Rothschild *et al*. [14] showed that Fe^{3+} was the dominant valence state in STF over a range of pressures and temperatures including those corresponding to the growth conditions, i.e. the composition can be written $SrTi_{1-x}Fe_xO_{3-(x/2)-\gamma}$ with γ representing the deviation from a state containing all Fe^{3+}. The presence of Fe^{2+} became significant at extremely low oxygen pressures, e.g., below 10^{-9} Torr at 600°C, whereas Fe^{4+} was present at higher pressures, e.g., above 10 mTorr. Rodriguez *et al*. showed that a mixture of Fe^{3+} and Fe^{4+} was present in STF after synthesis at 1300°C in oxygen [76], and Ferreira suggested that some Fe^{4+} was present at room temperature [20]. It is not clear how well the PLD growth conditions correspond to these equilibrium conditions, but we expect that the oxygen content will be kinetically trapped after cooling the samples from the growth temperature, implying that the oxygen content and the average Fe valence state in the films will be lower for films grown at a lower base pressure.

The formation of sparsely distributed metallic Fe nanorods was inferred in the P = 2 μTorr and 4 μTorr STF/STO samples. This was not seen in our previous work on STF [16], but there have been several other observations of metallic transition metal nanorods forming in an oxide matrix, notably Fe in a (non-perovskite) $LaSrFeO_4$ matrix formed from the deposition of $LaSr_{0.5}Fe_{0.5}O_3$, and Co, Ni or Fe in ceria or STO by codeposition of the matrix phase with a transition metal oxide [77-79]. In the P = 4 μTorr STF/STO, it is possible that the low base pressure combined with the large tetragonal distortion due to epitaxy promotes the precipitation of a fraction of the Fe as a strain relief mechanism that was not seen in the non-epitaxial films on Si. The precipitation of the small volume fraction of metallic Fe would lead to an excess of Sr in the perovskite matrix that could be accommodated through additional SrO layers as in Ruddlesden-Popper phases without disrupting the overall perovskite structure. In contrast, in the films on Si it appears that all the Fe was present within the perovskite lattice. The Fe distribution did, however, become less homogeneous at low base pressure. It is not clear why the STF unit cell volumes decreased for P < 4 μTorr. This may indicate a different strain relaxation mechanism becoming important, or a structural change due to the ordering of vacancies or the formation of Ti^{3+}.

In previous work, we have suggested that oxygen-deficient STF exhibits mixed valence Fe ions, leading to both ferromagnetic and antiferromagnetic interactions between nearest-neighbors. A range of other Fe-based perovskites including Sr_2FeMoO_6 and Ba_2FeReO_6 also display room temperature magnetism that originates on the Fe spins [80-82]. Moreover, the magnetic moment of Fe ions is dramatically affected by adjacent oxygen vacancies that break the symmetry of the oxygen coordination octahedron, as predicted theoretically in STCo [83]. Film strain leads to magnetoelastic anisotropy, which can orient the overall direction of magnetization in the film, accounting for the out-of-plane easy axis for STF/STO [16]. The resulting net magnetic moment of the STF and the hysteresis behavior is therefore highly dependent on the concentration and arrangement of the oxygen and Fe and the strain state, as well as the presence of Fe nanorods, and is expected to vary with all the film deposition conditions including P. In STCo, changes in P were also found to affect the magnetic moment [22].

The most striking finding in the present work is the higher magnetization and FR in films made on Si compared to those on STO. The films differ in their microstructure and strain state, but may also have subtle differences in oxygen content, vacancy clustering, or Fe distribution despite being deposited simultaneously; this could result from different surface kinetics or surface chemistry dur-

ing film nucleation, or differing substrate temperatures due to the differences in emissivity and thermal conductivity between the Si and STO substrates. The magnetic effects in STF/Si appear not to originate from metallic Fe, and are therefore intrinsic to the substituted perovskite. Metallic behavior has been calculated for STO surfaces [84], suggesting that the grain boundaries in the STF may play a role in its electronic properties. Unlike the STF/STO, which has a significant tetragonal distortion ($c/a > 1$) leading to magnetoelastic anisotropy [27,85], the polycrystalline STF/Si has little strain, suggesting that the origin of its magnetism is microstructural (influenced by grain boundaries, oxygen content, vacancy clustering, or the inhomogeneous Fe distribution observed in Figs. 2(a-c) and 3(b)) rather than magnetoelastic.

III. INTEGRATED MAGNETOOPTICAL ISOLATOR

The polycrystalline STF/Si is suitable for magnetooptical devices because it is expected to grow on a variety of substrates and it has a large remanent Faraday rotation angle. As an illustration of the integration of polycrystalline STF into a magneto-optical device, a ring resonator was prepared from a silicon-on-insulator wafer consisting of a racetrack placed adjacent to a straight waveguide, similar to the devices shown in Refs. [4,5] When light passing through the waveguide is resonant with the racetrack (i.e., when the racetrack circumference is an integral number of wavelengths), the light couples into the racetrack, and there is a drop in transmittance through the waveguide, as shown in Fig. 8. If the racetrack is clad on top with a magneto-optical material magnetized perpendicular to the waveguide, the transverse magnetic (TM) mode, but not the transverse electric (TE) mode, experiences a nonreciprocal phase shift (NRPS). This leads to a different resonant wavelength for clockwise and counterclockwise propagating TM light, which forms the basis of an isolator.

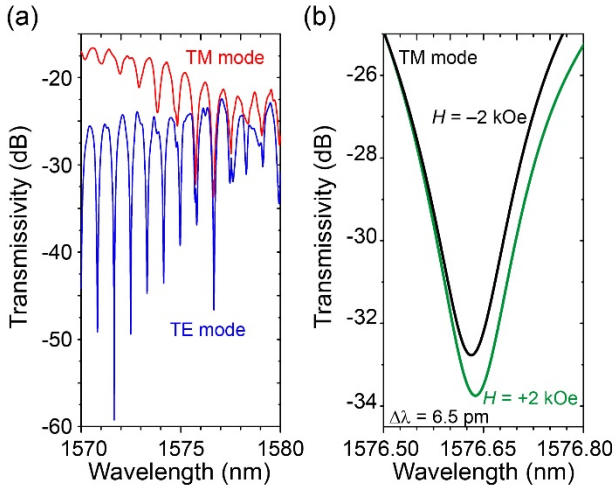

FIG. 8. Integration of STF on a waveguide device. (a) Resonant peaks for TE and TM modes at wavelengths between 1570 nm and 1580 nm. (b) Example of a peak shift for the TM mode that showed a NRPS of 6.5 nm when the field H direction was reversed.

The waveguides had a thickness of 250 nm and a width of 450 nm. The racetrack was 290 μm long and 90 μm wide. A 200-μm-long, 20-μm-wide window was opened in the silica cladding of one of the sides of the racetrack and STF (at $P = 4$ μTorr) was deposited over the sample, so that the STF contacted the waveguide directly within the window. The transmittance of the waveguide/resonator was measured at a wavelength of around 1550 nm for a magnetic field of ±2 kOe applied in-plane, perpendicular to the side of the racetrack. The resonant wavelength of both the TM and TE modes varied between successive measurements by up to 10 pm because of thermal drift or vibration, but the TM mode showed an NRPS of ~4 pm compared to the TE mode when the sign of the applied field was changed.

Similar devices made with CeYIG cladding [5] (FR ~–1300 °cm^{-1}) with in-plane magnetization exhibited a NRPS of ~20 pm. The lower NRPS in the STF devices is a result of incomplete in-plane saturation, which requires a field > 5 kOe. Based on the hysteresis loops, a 2 kOe in-plane field would lead to an in-plane magnetization of approximately 1/3 of the saturation magnetization. The FR scales with the magnetization, so we expect the STF to produce an NRPS of 1/3 of what would be produced at in-plane saturation. The NRPS of the STF devices is in reasonable agreement with the expected NRPS, considering the geometry of the resonator and the magnitude of the FR. The absorption of the STF at a wavelength of $\lambda = 1550$ nm was 31 ± 2 dB cm^{-1}, derived as shown in [69]. Hence, the figure of merit defined as the ratio of saturation FR/absorption was 58 °dB^{-1}, which is good compared with other thin film magneto-optical materials [17,33].

IV. ELECTRONIC STRUCTURE CALCULATIONS

We now present a brief discussion of the theoretical predictions for the electronic structure and the change of the lattice parameters as a function of the chemical pressure created by oxygen vacancies of STF based on hybrid density functional theory (DFT) [83], as described in the methods section. All possible vacancy and Fe configurations for STF with x = 0.125 or 0.25 were evaluated.

From Fig. 9(a), we find that STF with δ = 0.125 and x = 0.125 (one Fe atom and one vacancy in the 2×2×2 perovskite supercell) is a semiconductor with a band gap of ~1.1 eV. The e_g orbitals are partially occupied, which gives rise to the ferrimagnetism. From molecular orbital theory, we find that the high-low spin-gap energy is ~70 meV, which is actually larger than the ~40 meV required to take a spin to the e_g from the t_{2g} level [30]. A detailed analysis of the spin states in this system will be discussed in a subsequent publication. We confirmed the oxidation states were Fe^{2+} and Ti^{4+} rather than both ions being 3+, and the Ti^{4+} magnetic moment is negligible.

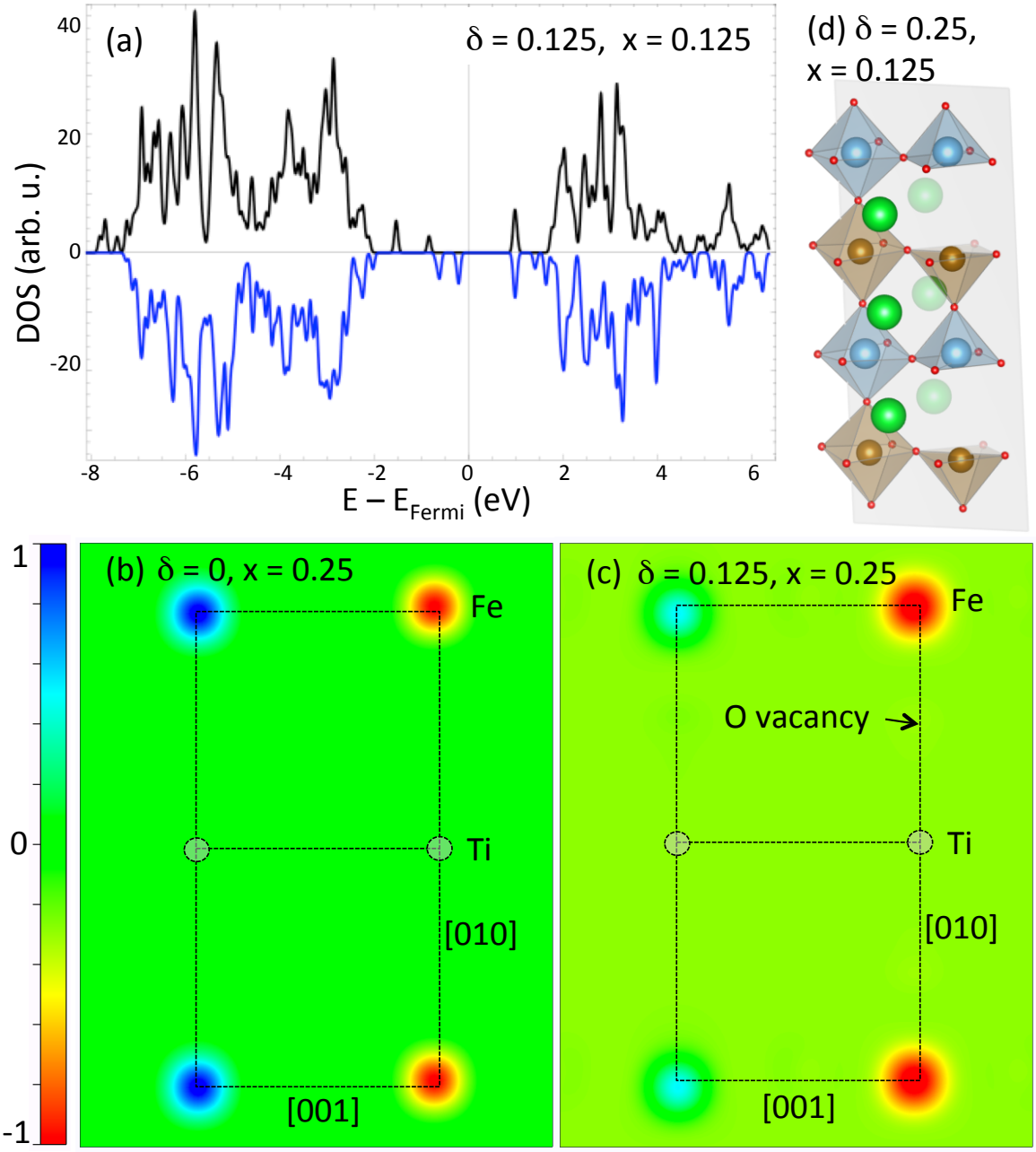

FIG. 9. DFT calculations. (a) Total density of states for $SrTi_{0.875}Fe_{0.125}O_{2.875}$ (high spin Fe) obtained with HSE06. The supercell contains one Fe ion and one neighboring vacancy. (b) Spin density (HSE) projected onto the (100) plane for $SrTi_{0.75}Fe_{0.25}O_3$ in which the two nearest-neighbor Fe ions are aligned in the [001] direction, showing clearly their antiferromagnetic ordering. (c) Spin densi-

ty (HSE) projected onto the (100) plane for $SrTi_{0.75}Fe_{0.25}O_{2.875}$ with an oxygen vacancy adjacent to one of the two Fe ions per unit cell. In both cases (b) and (c), the second-nearest Fe neighbors are also depicted and the color scale indicates the spin density normalized to the largest magnetic moment. The ferrimagnetic order in the O-deficient system is clear in (c). (d) Image showing the model in (c) in which the atomic positions are visible. The plane shown in (c) bisects the model passing through the Fe and Ti sites. Blue: Fe; brown: Ti; green: Sr; red: O.

When $x = 0.25$, the two Fe ions can be arranged along [001], [110], or [111]. In each case, the Fe-Fe distances are ~0.9x the Ti-Ti distance in STO, and the final unit cell is distorted from cubic symmetry. In the $\delta = 0$ case the Fe ions have an average moment of 3.7 μ_B, with an antiferromagnetic (AF) ground state in the Fe-[001] arrangement. For the [110] and [111] arrangements where the Fe ions are further separated, the lowest energy ferromagnetic (FM) and antiferromagnetic (AF) states are almost degenerate within a small energy range < 40 meV. The preponderance of [110] and [111] configurations in a crystal with random Fe site distribution suggests an overall low moment due to dominant AF interactions.

An oxygen vacancy ($\delta = 0.125$) leads to a significant increase in the volume of the unit cell compared to $\delta = 0$, in agreement with experiment. The volume increase is not due to the Fe-Fe interaction but to the chemical pressure created by the vacancy. When calculating the ground state for $\delta = 0.125$, the spin and valence of the two Fe ions were initialized in all possible combinations (i.e. both Fe^{3+}, one Fe^{4+} and one Fe^{2+}, high and low spin, and FM and AF) and the lowest energy state after relaxation was defined as the ground state. The low spin states tended to shift to high spin with ~ 4.1–4.2 μ_B, with the two Fe spins coupled AF in most but not all cases. However, even the AF-initialized cells had a net moment, i.e., they were ferrimagnetic, because the spin at each Fe location was not identical owing to their different locations with respect to the oxygen vacancy.

In the Fe-[001] case, the lowest energy configuration is one where the vacancy is between the two Fe ions, which eliminates the superexchange between the Fe ions that coordinate the vacancy. The magnetic moment was ~0.2 μ_B/Fe. In the Fe-[110] case, the two possible vacancy positions lead to similar energies, and the magnetization in the ground state is 0.3–0.4 μ_B/Fe. In the more symmetric case of Fe-[111], the FM and AF configurations are almost degenerate (i.e., < 0.1 meV) because of the large separation between the Fe atoms. The final magnetic moment of the AF-initialized arrangement is once again 0.1–0.2 μ_B/Fe.

To better understand the effects of the vacancies on the magnetic behavior, we calculate the HSE spin density for a system with x = 0.25 and $\delta = 0$ or $\delta = 0.125$. Figure 9(b) shows the spin density projected onto the (100) plane for $SrTi_{0.75}Fe_{0.25}O_3$ in which the two Fe ions are aligned in the [001] direction. The AF ordering of the two Fe ions is seen from the opposite sign but equal value of the spin density. In Fig. 9(c), a vacancy is introduced, i.e. the composition is $SrTi_{0.75}Fe_{0.25}O_{2.875}$ with the vacancy placed adjacent to one Fe ion but not between the two Fe ions. The magnetic moment of the Fe next to the vacancy is enhanced, as evident by the slightly larger radius of the red spin-density projections, while the other Fe which is completely O-coordinated has a smaller magnetic moment (blue) coupled antiferrimagneticaly to the larger moment of the first Fe. While the two Fe magnetic moments per unit cell in the first case are equal in magnitude, in the O-coordinated Fe case there is a difference of 0.1-0.3 μ_B/Fe between the moments (i.e. the system is ferrimagnetic), in accordance with our previous discussion. These results have been qualitatively confirmed using LMTO (linear muffin-tin orbital). In the case of Fig. 9(c) the magnetic moment of the incompletely coordinated Fe was higher, and this is the case for most of the possible combinations of Fe valence and spin state. However, a few configurations with a slightly higher energy showed an increase of the moment of both Fe ions or even an increase just of the magnetic moment of the completely coordinated Fe ion.

The STF film is expected to comprise randomly distributed Fe ions and vacancies, and we would therefore expect a variety of nearest neighbor configurations and resulting interactions to be present, including those addressed in the modeling. The crystal would then exhibit a relatively low net magnetic moment, dominated by AF coupling, analogous to a ferrimagnet but without long range order. The presence of vacancies is predicted to increase the unit cell volume, raise the magnetic moment at the Fe sites and to lead to a net moment even when AF interactions are dominant. These predictions are broadly in line with the experimental results.

V. CONCLUSION

In conclusion, STF ($SrTi_{0.65}Fe_{0.35}O_{3-\delta}$) films grown on Si or STO substrates by PLD showed a strong dependence of microstructure and magnetic properties on the base pressure during deposition. At an optimum base pressure for deposition ($P = 4$ μTorr) the films showed room temperature magnetism of up to 0.53 μ_B/Fe with out-of-plane magnetic anisotropy, and a coercivity of 3 kOe as well as a FR of –1900 °cm^{-1} at a wavelength of 1550 nm. STF grown on STO at the optimum base pressure of $P = 4$ μTorr showed a low (< 0.5%) volume fraction of metallic Fe nanorods not present at other pressures that contribute to the magnetic signal, but the polycrystalline STF films grown on Si showed 65% greater magnetization and FR compared to the epitaxial films on STO. There was no evidence of metallic Fe in the STF/Si, indicating that the magnetic and magneto-optical properties are intrinsic to the substituted perovskite. Polycrystalline STF was grown onto a silicon ring resonator, and its FR produced a non-reciprocal phase shift.

First-principles calculations showed that oxygen vacancies increase both the unit cell volume and the magnetic moment of the Fe ions. The dominant interactions are antiferromagnetic, leading to a material with a net magnetization below about 0.5 μ_B/Fe, which is reasonable compared with the experimental data. These results illustrate the important role of oxygen vacancies in determining the magnetic properties and structure of a Fe-substituted perovskite, and the integration of the perovskite in magneto-optical devices.

APPENDIX A: TARGET PREPARATION

$SrCO_3$ (99.99%), TiO_2 (99.99%) and Fe_2O_3 (hematite, 99.945%) powders were stoichiometrically mixed, ball milled for 24 hours, and calcined at 1200°C for 5 hours, showing a single perovskite phase. The powder was pressed into a 1-inch-diameter pellet and sintered at 1300°C for 5 hours.

APPENDIX B: SAMPLE PREPARATION FOR TEM

The samples were prepared using a focused ion beam (FEI-600), and then imaged on a JEOL 2010F field emission TEM at 200 kV acceleration voltage. The element distribution in the sample was mapped by STEM EDX.

APPENDIX C: X-RAY DIFFRACTION

For STF/STO, the PANAlytical X'pert was used. The wavelength was Cu-Kα (λ = 1.540598 Å), the source current was 40 mA, the voltage was 45 kV, and the scan step in 2θ was 0.017°. There was no offset of ω. For STF/STO reciprocal space maps, the Bruker-Axs D8 DISCOVER was used with Cu-Kα radiation. The x-ray beam was monochromated with the Ge(220)×4 and the Gobel mirror slit was 0.8 mm. The first and second monochromator slits were 0.2 mm and 1 mm. For STF/Si, the Rigaku Smartlab was used because of its capability for in-plane GID. The wavelength was Cu-Kα with a tube current of 200 mA and a voltage of 45 kV. The step of the 2θ goniometer was 0.024°, and the incident angle of the x-rays ω was fixed at 0.4°.

APPENDIX D: MÖSSBAUER SPECTROSCOPY

^{57}Fe Mössbauer spectroscopy with a ^{57}Co/Rh source (of approximately 20 mCi of activity) was performed at 300 K in order to characterize the iron in the samples using the conversion electron mode. The films were first metallized with a thin layer of aluminum (~30–40 nm) to provide a good Ohmic contact and subsequently inserted into the cathode structure of a He-CH_4 filled (5% at 1.7 bar) gas-flow proportional counter, for measurements lasting approximately one week in each case. Energy filtering enabled Mössbauer spectra were acquired for the film (deep electrons and x-rays) and primarily from the surface (~20–30 nm penetration depth, due to Auger electrons) for the sample on STO. No Mössbauer signal could be resolved for the lowest escape energies. The sample on Si had a weaker signal and no energy filtering was performed so the data corresponded to the full thickness. The spectra were fitted using the standard least-squares method, using a pure Fe metal foil for velocity calibration.

APPENDIX E: THEORETICAL METHOD

We performed spin-polarized DFT calculations with a Heyd-Scuseria-Ernzerhof (HSE) functional [86,87] as implemented in the Vienna Ab initio Simulation Package (VASP) and within a PAW-PBE framework [88]. Compared to semi-local DFT methods, HSE improves the accuracy of standard local magnetic moments as well as features of interest such as valence spin states, band–gaps, and lattice parameters, as shown previously for $SrCoO_3$ and $SrTiCoO_3$ [83]. A 2×2×2 perovskite supercell with 39 or 40 atoms for $\delta = 0$ or 0.125, respectively, was used. Monkhorst *k*-point meshes of 2×2×2 and 4×4×4 were used for relaxation and static calculations, respectively. The energy cutoff used was 500 eV, and forces were converged to within 10^{-5} eV Å^{-1}.

We explored all possible FM and AFM initializations in both high and low spin configurations for different combinations of valence states for Fe, i.e., 4 and $0\mu_B$ (high and low spin Fe^{2+}), 5 and $1\mu_B$ (high and low spin Fe^{3+}), and 4 and $2\mu_B$ (high and low spin Fe^{4+}). We also explored perturbations of ± 20%μ_B for every initialization. In total, a few hundred calculations were performed, and in all cases, the magnetic moments were allowed to fully relax to their final value. Some cases with 4 x 4 x 4 supercells were also examined with x = 0.25 and $\delta = 0.125$, of which a few reached convergence within a reasonable time. These configurations showed antiferromagnetic coupling between the Fe moments and agreed with the 2x2x2 supercell results.

ACKNOWLEDGMENT

TG acknowledges support from the JST PRESTO, JSPS Postdoctoral Fellowships for Research Abroad, Grant-in-Aid for Young Scientists (A) No. 26706009, and Challenging Exploratory Research No. 26600043. CR acknowledges support from the NSF DMR1419807 and ECCS 1607865 and from FAME, a SRC STARnet Center supported by DARPA and MARCO. MI acknowledges support from the JSPS Grant-in-Aid for Scientific Research (S) No. 26220902. This work utilized the shared experimental facilities of the Center for Materials Science and Engineering (CMSE), award NSF DMR1419807. We thank Prof. Lei Bi (University of

Electronic Science and Technology of China), Dr. Vivek Singh (MIT), Prof. Lionel C. Kimerling (MIT), and Mr. Masahiko Watanabe (Elionix) for experimental support and discussions.

REFERENCES

441 [1] J. Wang, J. B. Neaton, H. Zheng, V. Nagarajan, S. B. Ogale, B. Liu, D. Viehland, V. Vaithyanathan,
442 D. G. Schlom, U. V. Waghmare, N. A. Spaldin, K. M. Rabe, M. Wuttig, and R. Ramesh, Epitaxial $BiFeO_3$
443 multiferroic thin film heterostructures, Science **299**, 1719, (2003).
444 [2] G. Rijnders and D. H. A. Blank, Materials science: build your own superlattice, Nature **433**, 369,
445 (2005).
446 [3] A. Gozar, G. Logvenov, L. F. Kourkoutis, A. T. Bollinger, L. A. Giannuzzi, D. A. Muller, and I.
447 Bozovic, High-temperature interface superconductivity between metallic and insulating copper oxides,
448 Nature **455**, 782, (2008).
449 [4] L. Bi, J. Hu, P. Jiang, D. H. Kim, G. F. Dionne, L. C. Kimerling, and C. A. Ross, On-chip optical
450 isolation in monolithically integrated non-reciprocal optical resonators, Nat. Photon. **5**, 758, (2011).
451 [5] T. Goto, M. C. Onbasli, D. H. Kim, V. Singh, M. Inoue, L. C. Kimerling, and C. A. Ross, A
452 nonreciprocal racetrack resonator based on vacuum-annealed magnetooptical cerium-substituted yttrium
453 iron garnet, Opt. Express **22**, 19047, (2014).
454 [6] G. M. Choi, H. L. Tuller, and D. Goldschmidt, Electronic-transport behavior in single-crystalline
455 $Ba_{0.03}Sr_{0.97}TiO_3$, Phys. Rev. B **34**, 6972, (1986).
456 [7] J. H. Haeni, P. Irvin, W. Chang, R. Uecker, P. Reiche, Y. L. Li, S. Choudhury, W. Tian, M. E. Hawley,
457 B. Craigo, A. K. Tagantsev, X. Q. Pan, S. K. Streiffer, L. Q. Chen, S. W. Kirchoefer, J. Levy, and D. G.
458 Schlom, Room-temperature ferroelectricity in strained $SrTiO_3$, Nature **430**, 758, (2004).
459 [8] A. Ohtomo and H. Y. Hwang, A high-mobility electron gas at the $LaAlO_3/SrTiO_3$ heterointerface,
460 Nature **427**, 423, (2004).
461 [9] A. D. Caviglia, S. Gariglio, N. Reyren, D. Jaccard, T. Schneider, M. Gabay, S. Thiel, G. Hammerl, J.
462 Mannhart, and J. M. Triscone, Electric field control of the $LaAlO_3/SrTiO_3$ interface ground state, Nature
463 **456**, 624, (2008).
464 [10] K. Ueno, S. Nakamura, H. Shimotani, A. Ohtomo, N. Kimura, T. Nojima, H. Aoki, Y. Iwasa, and M.
465 Kawasaki, Electric-field-induced superconductivity in an insulator, Nat. Mater. **7**, 855, (2008).
466 [11] W. Jung and H. L. Tuller, Impedance study of $SrTi_{1-x}Fe_xO_{3-\delta}$ (x = 0.05 to 0.80) mixed ionic-electronic
467 conducting model cathode, Solid State Ionics **180**, 843, (2009).
468 [12] W. Jung and H. L. Tuller, Investigation of cathode behavior of model think-film $SrTi_{1-x}FexO_{3-}$ (x =
469 0.35 and 0.5) mixed ionic-electronic conducting electrodes, J. Electrochem. Soc. **155**, B1194, (2008).
470 [13] L. H. Brixner, Preparation and properties of the $SrTi_{1-x}Fe_xO_{3-x/2}O_{x/2}$ system, Mater. Res. Bullet. **3**,
471 299, (1968).
472 [14] A. Rothschild, W. Menesklou, H. L. Tuller, and E. Ivers-Tiffée, Electronic structure, defect chemistry,
473 and transport properties of $SrTi_{1-x}Fe_xO_{3-y}$ solid solutions, Chem. Mater. **18**, 3651, (2006).
474 [15] D. P. Fagg, V. V. Kharton, A. V. Kovalevsky, A. P. Viskup, E. N. Naumovich, and J. R. Frade, The
475 stability and mixed conductivity in La and Fe doped $SrTiO_3$ in the search for potential SOFC anode
476 materials, J. Eur. Ceram. Soc. **21**, 1831, (2001).
477 [16] D. H. Kim, L. Bi, P. Jiang, G. F. Dionne, and C. A. Ross, Magnetoelastic effects in $SrTi_{1-x}M_xO_3$ (M =
478 Fe, Co, or Cr) epitaxial thin films, Phys. Rev. B **84**, 014416, (2011).
479 [17] H.-S. Kim, L. Bi, G. F. Dionne, and C. A. Ross, Magnetic and magneto-optical properties of Fe-doped
480 $SrTiO_3$ films, Appl. Phys. Lett. **93**, 092506, (2008).
481 [18] Y. G. Wang, X. G. Tang, Q. X. Liu, Y. P. Jiang, and Z. Y. Feng, Ferroelectric and ferromagnetic
482 properties of $SrTi_{0.9}Fe_{0.1}O_{3-\delta}$ thin films, Solid State Commun. **202**, 24, (2015).
483 [19] H.-S. Kim, L. Bi, D. H. Kim, D.-J. Yang, Y. J. Choi, J. W. Lee, J. K. Kang, Y. Chang Park, G. F.
484 Dionne, and C. A. Ross, Ferromagnetism in single crystal and nanocomposite $Sr(Ti,Fe)O_3$ epitaxial films, J.
485 Mater. Chem. **21**, 10364, (2011).
486 [20] A. A. L. Ferreira, J. C. C. Abrantes, J. R. Jurado, and J. R. Frade, Oxygen stoichiometry of
487 $Sr_{0.97}(Ti,Fe)O_{3-\delta}$ materials, Solid State Ionics **135**, 761, (2000).
488 [21] M. Kuhn, J. J. Kim, S. R. Bishop, and H. L. Tuller, Oxygen nonstoichiometry and defect chemistry of
489 perovskite-structured $Ba_xSr_{1-x}Ti_{1-y}Fe_yO_{3-y/2+\delta}$ solid solutions, Chem. Mater. **25**, 2970, (2013).
490 [22] S. Steinsvik, R. Bugge, J. O. N. GjØnnes, J. TaftØ, and T. Norby, The defect structure of
491 $SrTi_{1-x}Fe_xO_{3-Y}$ (x = 0–0.8) investigated by electrical conductivity measurements and electron energy loss
492 spectroscopy (EELS), J. Phys. Chem. Solids **58**, 969, (1997).
493 [23] V. V. Kharton, A. V. Kovalevsky, A. P. Viskup, F. M. Figueiredo, J. R. Frade, A. A. Yaremchenko,
494 and E. N. Naumovich, Faradaic efficiency and oxygen permeability of $Sr_{0.97}Ti_{0.6}0Fe_{0.4}0O_{3-\delta}$ perovskite, Solid
495 State Ionics **128**, 117, (2000).

[24] J. R. Jurado, F. M. Figueiredo, B. Gharbage, and J. R. Frade, Electrochemical permeability of $Sr_{0.7}(Ti,Fe)O_{3-\delta}$ materials, Solid State Ionics **118**, 89, (1999).
[25] L. A. Errico, M. Rentería, and M. Weissmann, Theoretical study of magnetism in transition-metal-doped TiO_2 and $TiO_{2-\delta}$, Phys. Rev. B **72**, 184425, (2005).
[26] L. Bi, H.-S. Kim, G. F. Dionne, and C. A. Ross, Structure, magnetic properties and magnetoelastic anisotropy in epitaxial $Sr(Ti_{1-x}Co_x)O_3$ films, New J. Phys. **12**, 043044, (2010).
[27] D. H. Kim, N. M. Aimon, L. Bi, G. F. Dionne, and C. A. Ross, The role of deposition conditions on the structure and magnetic properties of $SrTi_{1-x}Fe_xO_3$ films, J. Appl. Phys. **111**, 07A918, (2012).
[28] D. H. Kim, N. M. Aimon, L. Bi, J. M. Florez, G. F. Dionne, and C. A. Ross, Magnetostriction in epitaxial $SrTi_{1-x}Fe_xO_{3-\delta}$ perovskite films with x = 0.13 and 0.35, J. Phys.: Condens. Matter **25**, 026002, (2013).
[29] G. F. Dionne, *Magnetic oxides* (Springer Berlin Heidelberg, New York, 2009).
[30] G. F. Dionne, Evidence of magnetoelastic spin ordering in dilute magnetic oxides, J. Appl. Phys. **101**, 09C509, (2007).
[31] H.-S. Kim, L. Bi, H. Paik, D.-J. Yang, Y. C. Park, G. F. Dionne, and C. A. Ross, Self-assembled single-phase perovskite nanocomposite thin films, Nano Lett. **10**, 597, (2010).
[32] M. Shone, The technology of YIG film growth, Circ. Syst. Signal Process. **4**, 89, (1985).
[33] M. C. Onbaşlı, T. Goto, A. Tang, A. Pan, E. Battal, A. K. Okyay, G. F. Dionne, and C. A. Ross, Oxygen partial pressure dependence of magnetic, optical and magneto-optical properties of epitaxial cobalt-substituted $SrTiO_3$ films, Opt. Express **23**, 13399, (2015).
[34] N. H. Perry, J. J. Kim, S. R. Bishop, and H. L. Tuller, Strongly coupled thermal and chemical expansion in the perovskite oxide system $Sr(Ti,Fe)O_{3-\delta}$, J. Mater. Chem. A **3**, 3602, (2015).
[35] T. Goto, A. V. Baryshev, K. Tobinaga, and M. Inoue, Faraday rotation of a magnetophotonic crystal with the dual-cavity structure, J. Appl. Phys. **107**, 09A946, (2010).
[36] T. Goto, A. V. Dorofeenko, A. M. Merzlikin, A. V. Baryshev, A. P. Vinogradov, M. Inoue, A. A. Lisyansky, and A. B. Granovsky, Optical Tamm states in one-dimensional magnetophotonic structures, Phys. Rev. Lett. **101**, 113902, (2008).
[37] M. Levy, R. M. Osgood, Jr., H. Hegde, F. J. Cadieu, R. Wolfe, and V. J. Fratello, Integrated optical isolators with sputter-deposited thin-film magnets, IEEE Photon. Technol. Lett. **8**, 903, (1996).
[38] M. C. Onbasli, T. Goto, X. Sun, N. Huynh, and C. A. Ross, Integration of bulk-quality thin film magneto-optical cerium-doped yttrium iron garnet on silicon nitride photonic substrates, Opt. Express **22**, 25183, (2014).
[39] I. L. Lyubchanskii, N. N. Dadoenkova, M. I. Lyubchanskii, E. A. Shapovalov, A. E. Zabolotin, Y. P. Lee, and T. Rasing, Response of two-defect magnetic photonic crystals to oblique incidence of light: Effect of defect layer variation, J. Appl. Phys. **100**, 096110, (2006).
[40] T. Goto, R. Isogai, and M. Inoue, Para-magneto- and electro-optic microcavities for blue wavelength modulation, Opt. Express **21**, 19648, (2013).
[41] T. Goto, R. Hashimoto, R. Isogai, Y. Suzuki, R. Araki, H. Takagi, and M. Inoue, Fabrication of microcavity with magneto- and electro-optical film, J. Magn. Soc. Jpn. **36**, 197, (2012).
[42] M. Inoue, M. Levy, and A. V. Baryshev, *Magnetophotonics from theory to applications* (Springer Berlin Heidelberg, New York, 2014).
[43] G. Fan, K. Pennington, and J. H. Greiner, Magneto - Optic Hologram, J. Appl. Phys. **40**, 974, (1969).
[44] R. Isogai, S. Suzuki, K. Nakamura, Y. Nakamura, H. Takagi, T. Goto, P. B. Lim, and M. Inoue, Collinear volumetric magnetic holography with magnetophotonic microcavities, Opt. Express **23**, 13153, (2015).
[45] H.-Y. S. Li and D. Psaltis, Three-dimensional holographic disks, Appl. Opt. **33**, 3764, (1994).
[46] H. J. Coufal, D. Psaltis, and G. T. Sincerbox, *Holographic Data Storage* (Springer, New York, 2000).
[47] L. Bi, J. Hu, G. F. Dionne, L. Kimerling, and C. A. Ross, in *Proceedings of the SPIE*, edited by J. E. Broquin, and G. N. Conti (SPIE, San Francisco, California, USA, 2011), pp. 5.
[48] H. E. Swanson, G. M. Ugrinic, R. K. Fuyat, and S. United, *Standard x-ray diffraction powder patterns. Vol. III, Data for 34 inorganic substances* (National Bureau of Standards, Washington, D.C., 1954), p. 44.
[49] I. D. Zhitomirskii, O. I. Chechernikova, V. V. Ivanova, and Y. N. Venevtsev, $(Pb_xSr_{1-x})(Fe_{2/3}Te_{1/3})O_3$ and $Sr[Fe_{2/3}(Te_xW_{1-x})_{1/3}]O_3$ solid solutions, Inorg. Mater. **19**, 849, (1983).
[50] T. Ohnishi, K. Shibuya, T. Yamamoto, and M. Lippmaa, Defects and transport in complex oxide thin

films, J. Appl. Phys. **103**, 103703, (2008).
[51] J. B. MacChesney, R. C. Sherwood, and J. F. Potter, Electric and magnetic properties of the strontium ferrates, J. Chem. Phys. **43**, 1907, (1965).
[52] H. Taguchi, M. Shimada, and M. Koizumi, The effect of oxygen vacancy on the magnetic properties in the system $SrCoO_{3-\delta}$ ($0<\delta<0.5$), J. Solid State Chem. **29**, 221, (1979).
[53] S. Chakraverty, A. Ohtomo, M. Okude, K. Ueno, and M. Kawasaki, Epitaxial structure of (001)- and (111)-oriented perovskite ferrate films grown by pulsed-laser deposition, Cryst. Growth Des. **10**, 1725, (2010).
[54] S. Kuroda, N. Nishizawa, K. Takita, M. Mitome, Y. Bando, K. Osuch, and T. Dietl, Origin and control of high-temperature ferromagnetism in semiconductors, Nat. Mater. **6**, 440, (2007).
[55] T. Dietl, From our readers: Self-organized growth controlled by charge states of magnetic impurities, Nat. Mater. **5**, 673, (2006).
[56] M. Yokoyama, H. Yamaguchi, T. Ogawa, and M. Tanaka, Zinc-blende-type MnAs nanoclusters embedded in GaAs, J. Appl. Phys. **97**, 10D317, (2005).
[57] Y. Shimakawa, S. Inoue, M. Haruta, M. Kawai, K. Matsumoto, A. Sakaiguchi, N. Ichikawa, S. Isoda, and H. Kurata, Topotactic Changes in Thin Films of Brownmillerite $SrFeO_{2.5}$ Grown on $SrTiO_3$ Substrates to Infinite-Layer Structure $SrFeO_2$, Cryst. Growth Des. **10**, 4713, (2010).
[58] M. Sharma, J. Gazquez, M. Varela, J. Schmitt, and C. Leighton, Growth temperature control of the epitaxy, magnetism, and transport in $SrTiO_3(001)/La_{0.5}Sr_{0.5}CoO_3$ thin films, Journal of Vacuum Science & Technology A **29**, 051511, (2011).
[59] J. Gazquez, S. Bose, M. Sharma, M. A. Torija, S. J. Pennycook, C. Leighton, and M. Varela, Lattice mismatch accommodation via oxygen vacancy ordering in epitaxial $La_{0.5}Sr_{0.5}CoO_{3-\delta}$ thin films, APL Mater. **1**, 012105, (2013).
[60] T. C. Gibb, P. D. Battle, S. K. Bollen, and R. J. Whitehead, Investigation of the crystal and magnetic structure of the perovskite system Sr_2FeTiO_{6-y} by Mossbauer spectroscopy and neutron diffraction, J. Mater. Chem. **2**, 111, (1992).
[61] U. Gonser, *Mössbauer Spectroscopy* (Springer Berlin Heidelberg, 1975).
[62] U. Gonser, *Microscopic Methods in Metals* (Springer Berlin Heidelberg, 1986).
[63] F. E. Fujita, *Physics of New Materials* (Springer Berlin Heidelberg, 1998).
[64] W. Eerenstein, F. D. Morrison, J. Dho, M. G. Blamire, J. F. Scott, and N. D. Mathur, Comment on "Epitaxial $BiFeO_3$ Multiferroic Thin Film Heterostructures", Science **307**, 1203, (2005).
[65] T. Schedel-Niedrig, W. Weiss, and R. Schlögl, Electronic structure of ultrathin ordered iron oxide films grown onto Pt(111), Phys. Rev. B **52**, 17449, (1995).
[66] K. Sato, *Hikari-to-jiki* (Asakura-shoten, Tokyo, 2007), p. 92.
[67] T. Shintaku, A. Tate, and S. Mino, Ce-substituted yttrium iron garnet films prepared on $Gd_3Sc_2Ga_3O_{12}$ garnet substrates by sputter epitaxy, Appl. Phys. Lett. **71**, 1640, (1997).
[68] B. Stadler, K. Vaccaro, P. Yip, J. Lorenzo, L. Yi-Qun, and M. Cherif, Integration of magneto-optical garnet films by metal-organic chemical vapor deposition, IEEE Trans. Magn. **38**, 1564, (2002).
[69] T. Goto, Y. Eto, K. Kobayashi, Y. Haga, M. Inoue, and C. A. Ross, Vacuum annealed cerium-substituted yttrium iron garnet films on non-garnet substrates for integrated optical circuits, J. Appl. Phys. **113**, 17A939, (2013).
[70] T. Goto, M. C. Onbasli, and C. A. Ross, Magneto-optical properties of cerium substituted yttrium iron garnet films with reduced thermal budget for monolithic photonic integrated circuits, Opt. Express **20**, 28507, (2012).
[71] S. Higuchi, Y. Furukawa, S. Takekawa, O. Kamada, K. Kitamura, and K. Uyeda, Magnetooptical properties of cerium-substituted yttrium iron garnet single crystals for magnetic-field sensor, Sens. Actuators, A **105**, 293, (2003).
[72] C. Greaves and R. A. Buker, The defect structure of Sr_2FeTiO_{6-x}, Mater. Res. Bullet. **21**, 823, (1986).
[73] C. Yu, M. L. Scullin, M. Huijben, R. Ramesh, and A. Majumdar, The influence of oxygen deficiency on the thermoelectric properties of strontium titanates, Appl. Phys. Lett. **92**, 092118, (2008).
[74] D. A. Muller, N. Nakagawa, A. Ohtomo, J. L. Grazul, and H. Y. Hwang, Atomic-scale imaging of nanoengineered oxygen vacancy profiles in $SrTiO_3$, Nature **430**, 657, (2004).
[75] M. A. A. Franco and M. V. Regi, Anion deficiency in strontium titanate, Nature **270**, 706, (1977).
[76] J. Rodriguez, J. A. Pereda, M. Vallet, J. G. Calbet, and J. Tejada, Mössbauer study of vacancy ordering in the system $SrTi_{1-x}Fe_xO_{3-y}$ ($0.50 \le x \le 0.70$), Mater. Res. Bullet. **21**, 255, (1986).

[77] F. Vidal, Y. Zheng, J. Milano, D. Demaille, P. Schio, E. Fonda, and B. Vodungbo, Nanowires formation and the origin of ferromagnetism in a diluted magnetic oxide, Appl. Phys. Lett. **95**, 152510, (2009).
[78] P. Schio, F. Vidal, Y. Zheng, J. Milano, E. Fonda, D. Demaille, B. Vodungbo, J. Varalda, A. J. A. de Oliveira, and V. H. Etgens, Magnetic response of cobalt nanowires with diameter below 5 nm, Phys. Rev. B **82**, 094436, (2010).
[79] F. Vidal, P. Schio, N. Keller, Y. Zheng, D. Demaille, F. J. Bonilla, J. Milano, and A. J. A. de Oliveira, Magneto-optical study of slanted Co nanowires embedded in $CeO_2/SrTiO_3$(0 0 1), Physica B: Condensed Matter **407**, 3070, (2012).
[80] A. W. Sleight and J. F. Weiher, Magnetic and electrical properties of Ba_2MReO_6 ordered perovskites, J. Phys. Chem. Solids **33**, 679, (1972).
[81] T. Nakagawa, Magnetic and electrical properties of ordered perovskite $Sr_2(FeMo)O_6$ and its related compounds, J. Phys. Soc. Jpn. **24**, 806, (1968).
[82] B. García-Landa, C. Ritter, M. R. Ibarra, J. Blasco, P. A. Algarabel, R. Mahendiran, and J. García, Magnetic and magnetotransport properties of the ordered perovskite Sr_2FeMoO_6, Solid State Commun. **110**, 435, (1999).
[83] J. M. Florez, S. P. Ong, M. C. Onbaşli, G. F. Dionne, P. Vargas, G. Ceder, and C. A. Ross, First-principles insights on the magnetism of cubic $SrTi_{1-x}Co_xO_{3-\delta}$, Appl. Phys. Lett. **100**, 252904, (2012).
[84] A. R. Silva and G. M. Dalpian, Oxygen vacancies at the surface of SrTiO3 thin films, J. Appl. Phys. **115**, 033710, (2014).
[85] P. Adler, Charge disproportionation in iron(IV) oxides: electronic properties and magnetism in $Sr_3Fe_{2-x}Ti_xO_{7-y}$ annealed at high oxygen pressures, J. Mater. Chem. **9**, 471, (1999).
[86] J. Heyd, G. E. Scuseria, and M. Ernzerhof, Hybrid functionals based on a screened Coulomb potential, J. Chem. Phys. **118**, 8207, (2003).
[87] J. Heyd, G. E. Scuseria, and M. Ernzerhof, Erratum: "Hybrid functionals based on a screened Coulomb potential" [J. Chem. Phys.118, 8207 (2003)], J. Chem. Phys. **124**, 219906, (2006).
[87] G. Kresse and J. Furthmüller, Efficient iterative schemes for *ab initio* total-energy calculations using a plane-wave basis set, Phys. Rev. B **54**, 11169, (1996).